Research Square

Preprints are preliminary reports that have not undergone peer review.
They should not be considered conclusive, used to inform clinical practice,
or referenced by the media as validated information.

Unified design of interaction and field-guided transport in active Janus colloid systems

Xuemao Zhou

zhouxuemao@gxstnu.edu.cn

Guangxi Science & Technology Normal University https://orcid.org/0000-0002-3332-4445

Lijie Lei

Civil Aviation Flight University of China https://orcid.org/0000-0002-9105-5749

Weiqi Liu

Guangxi Science & Technology Normal University

Fei Yang

Guangxi Science & Technology Normal University

Shuo Wang

Shenzhen Technology University

Salah Eddine Ghellab

Chalmers University of Technology

Article

Keywords: Active colloids, Pair interaction, Light controlled motion, Swarming

Posted Date: May 19th, 2026

DOI: https://doi.org/10.21203/rs.3.rs-9515242/v1

License: This work is licensed under a Creative Commons Attribution 4.0 International License.
Read Full License

Additional Declarations: There is **NO** Competing Interest.

Unified design of interaction and field-guided transport in active Janus colloid systems

Xuemao Zhou[1*], Liejie Lei[2*], Weiqi Liu[1], Fei Yang[1], Shuo Wang[3], Salah Eddine Ghellab[4]

[1]School of Physics and Information Engineering, Guangxi Science and Technology Normal University, 966 Tiebei Ave., Laibin, 546199, Guangxi, China.

[2]College of Aviation Engineering, Civil Aviation Flight University of China, 46 Nanchang road, Guanghan, 618307, Sichuan, China.

[3]Julong College, Shenzhen Technology University, 3002 Lantian Road, Shenzhen, 518118, Guangdong, China.

[4]Division of Chemistry and Biochemistry, Department of Chemistry and Chemical Engineering, Chalmers University of Technology, Kemigården 4, Gothenburg, 412 96, Västra Götaland, Sweden.

*Corresponding author(s). E-mail(s): zhouxuemao@gxstnu.edu.cn; leilijie@cafuc.edu.cn;

Abstract

Active Janus colloids hold promise for targeted delivery and self-assembly, yet rational design of their motion remains challenging. Here, we present a unified model that treats Janus particles as coupled active-passive dimers with tunable mobility contrast, enabling predictive design of colloidal dynamics. This framework captures how surface anisotropy mediates coupling to shared gradient fields regardless of their origin, whether generated by neighboring particles or imposed externally. Based on this framework, we experimentally and in simulation demonstrate that intrinsically repulsive particles can be engineered to exhibit attractive interactions, forming long-lived three-particle swarms with emergent velocity enhancement up to fourfold via a concentration-slingshot mechanism. We further achieve light-guided motion of dumbbell particles within structured light fields, validating the model's predictive power for both interaction-mediated collective behavior and field-guided transport. Our study provides a unified approach to rationally engineering motions of active Janus colloids.

Keywords: Active colloids, Pair interaction, Light controlled motion, Swarming

Active colloids has been intensively studied for the last two decades due to their promising applications in biomedicine [1, 2], environmental remediation [3] and beyond[4]. They self-propel by responding to local gradient fields, with their motion controlled by communication with neighbors or the environment [4–6]. Existing frameworks for modeling such communication, including bispherical coordinate systems [7–10] and multipole expansions [11, 12], are mathematically complex limiting their applications beyond pair interactions. Experimental study remains challenging because the particle interaction depends not only on the surface distribution of mobility and activity, but also on how they encounter. Therefore, limited pair-wise dynamics has been experimentally explored, including paring and scattering [13–15], escaping [14], interacting with tethered particle [16, 17] and acceleration when encountered [18]. On the other hand, field-controlled transports have been explored using external body force [19–21], created chemical [22], electrical [23] or light[16, 24–26] gradient. However, a "bottom-up" paradigm for field-guided motion is yet to be developed.

Previous approaches decomposed interactions into background-free self-propulsion and phoretic drift from neighboring fields [14], and separated the external steering from the mechanism of propulsion [23, 27]. While this separation simplifies analysis, it inherently limits the control strategies to scenarios where propulsion and guidance are independent, thereby precluding the exploitation of synergistic effects that arise from the full coupling of gradient fields [28, 29]. A unified framework capturing how anisotropic particles respond to the total gradient field—whether generated by neighbors, imposed externally, or both—remains elusive, hindering rational design of colloidal systems that integrate both strategies.

Here we introduce a unified framework that resolves this challenge by modeling Janus particles as active-passive dimers. This approach captures the full coupling between self-generated and external fields, allowing us to predict and engineer interactions and boundary-guided transport in a shared gradient field.

1 Dimer model of interacting Janus particles

The interaction between two chemically driven active Janus colloids consists of self- and inter-part motions (Fig. 1a). The self-part originates from the self-generated concentration field: for axisymmetric particles, positive surface mobility $\mu > 0$ induces slip velocity aligned with the tangential concentration gradient $\nabla_{\|} c(\mathbf{r})$ at the particle surface, driving motion along the particle orientation (pointing from active to passive) [30–32]. The self-propulsion velocity $\mathbf{v} = -\frac{1}{S} \oint d\mathbf{r} \mu(\mathbf{r}) \nabla_{\|} c(\mathbf{r})$ corresponds to the average slip velocity over the surface area S.

To capture the inter-part motion, we model the Janus colloid as a dimer—an active sphere (radius r_{a}, mobility μ_{a}) and a passive sphere (radius r_{p}, mobility μ_{p}) separated by center-to-center distance d_{c}. This framework captures the essential physics

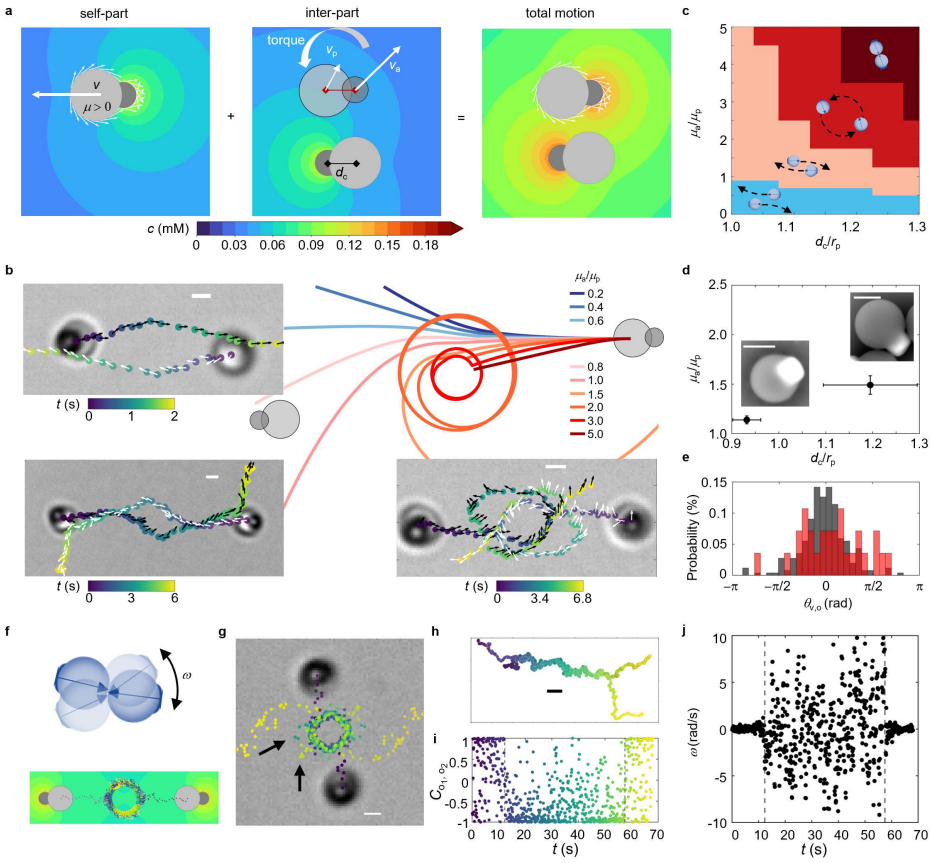


Fig. 1 Dimer model for attractive head-on scattering between repulsive Janus particles. **a** Dimer model of Janus particle interactions mediated by a gradient field. White arrows on particle surfaces are unit vectors indicating the direction of the concentration gradient. The middle schematic illustrates dimer–dimer interactions between two Janus particles with surface mobilities $\mu_a > \mu_p > 0$. **b** Athermal simulations trajectories of scattering Janus particles with $d_c/r_p = 1.2$ and varying μ_a/μ_p . Insets present experimental trajectories of weak (top left) and strong (bottom left) attractive scattering, and recapturing (bottom right) in the center-of-mass reference frame. Arrows indicates the particle orientation. **c** μ_a/μ_p vs. d_c/r_p state diagram from athermal simulation, showing repulsive scattering (blue), attractive scattering (pink), circling bound state (red) and head-to-head static state (dark red). **d** μ_a/μ_p vs. d_c/r_p parameter space of hematite/TPM Janus particles explored in experiments. Insets present SEM images of each particle type: hematite (white cube) is partially encapsulated by a TPM sphere (gray). **e** Probability distribution of $\theta_{v,o}$ when particle distance $d > 3r_p$ (black) and $d < 3r_p$ (red) during attractive scattering. **f** Schematic (top) and simulation trajectories (bottom) showing angular velocity about the center-of-mass in the head-to-head state with thermal fluctuations. **g, h** Experimental trajectories of particles in the head-to-head state: center-of-mass frame (**g**) and laboratory frame (**h**). Black arrows in **g** mark two scattering events. **i, j** Time evolution of the correlation between orientations C_{o_1,o_2} (**i**) and angular velocity ω in the head-to-head state. Dashed lines indicate the start and end of the head-to-head state. Scale bars: 1 μm (**b, d, g**); 10 μm (**h**).

of surface asymmetry: when $d_c \to 0$ and $r_a = r_p$, the dimer reduces to the classic half-coated Janus colloids[33]; varying d_c tunes morphology from snowman-like [34] to (hetero-)dumbbells [35]. In the low-Reynolds-number regime, average slip velocities on passive (active) surfaces generate forces $F \propto v_p$ (v_a) at their respective centers, leading to mutual repulsion for $\mu > 0$. When $v_p < v_a$, a counterclockwise torque is induced (Fig. 1a), resulting in attractive scattering; conversely, $v_p > v_a$ causes clockwise torque and repulsive scattering. Torque is tunable via the mobility contrast μ_a/μ_p and d_c. Compared to the motion of isolated particle (self-part) where the velocity aligns with particle orientation, interacting particles exhibit total velocity deviating from their orientation.

Based on the dimer model, we numerically represent the active and passive spheres by a point source and a dipole, respectively. This perspective leads to a 2D complex potential method, where the concentration field is obtained by superposing these two contributions (Methods). Unlike conventional multipole expansions that treat the entire particle as a series of singularities [11, 12], our approach directly captures the physical asymmetry between active and passive parts, enabling straightforward evaluation of the total concentration field experienced by all particles.

Unit vectors in Fig. 1a (total motion panel) indicate surface concentration gradients; comparison with the self-part panel reveals the distortion induced by neighboring particles. From the total concentration field, we determine the translational and rotational velocities of each particle.

2 Attractive head-on scattering from repulsive Janus colloids

We simulated the scattering trajectories of two approaching Janus colloids using athermal Brownian dynamics (Methods) at $d_c/r_p = 1.2$ and varying μ_a/μ_p for both particles (Fig. 1b and Supplementary Video S1). For $\mu_a/\mu_p < 0.8$, particles deflected away (repulsive scattering); above 0.8, scattering became attractive, with stronger attraction at higher mobility contrasts. Between $1.8 < \mu_a/\mu_p < 3.5$, particles circled each other, forming a bound state in the absence of thermal fluctuations. At $\mu_a/\mu_p > 3.5$, particles turned into a static head-to-head state with their passive faces touching, which is unexpected previously [11]. Steady state dynamics from athermal simulations were categorized in the μ_a/μ_p vs. d_c/r_p state diagram (Fig. 1c). For fixed μ_a/μ_p, increasing d_c enlarged the scattering angle — consistent with an extended lever arm (Fig. 1a, total motion panel).

To experimentally explore attractive scattering between inherently repulsive Janus particles, we fabricated hematite particles partially encapsulated with 3-trimethoxysilyl propyl methacrylate (TPM). Under UV illumination, the hematite part decomposes hydrogen peroxide creating a concentration field of diffusing H^+/OH^-, driving particle motion with passive (TPM) face leading [36, 37]. Two types of Janus particles with varying μ_a/μ_p and d_c/r_p were studied (Fig. 1d, Supplementary Sec. 1). Standard Janus particles (small d_c/r_p) exhibited weak-to-strong attractive scattering (inset, Fig. 1b; Supplementary Video S2), while dewetted particles (large d_c/r_p) formed circling pairs—though thermal fluctuations disrupted this

bound state, leading to recapturing behavior (bottom right, Fig. 1b; Supplementary Video S2). During scattering, the angle $\theta_{v,o}$ between velocity and orientation (hematite-to-TPM) distributed around 0 when particles were distant but deviated significantly at close proximity (Fig. 1e). It confirms our dimer model wherein near-field interactions misalign velocity and intrinsic orientation.

The head-to-head state was static in athermal simulations, but thermal fluctuations induced spinning about the center-of-mass (top, Fig. 1f). We introduced thermal noise ($D/D_0 = 0.05$; $D_0 = \alpha_0\mu_0/24\pi$, where α_0 and μ_0 are the surface activity and mobility of the active part; Methods) to demonstrate this behavior in simulation (bottom, Fig. 1f). Using dewetted particles, we experimentally verified long-lived head-to-head states (Fig. 1g,h; Supplementary Video S2): particles encountered at t = 12.3 s spun as they translated for >50 s. The correlation between two orientations C_{o_1,o_2} converged to -1 during this period (Fig. 1i), confirming mutual face-to-face alignment. The angular velocity ω of the dimer cluster oscillated between positive and negative values (Fig. 1j) — a signature distinguishing this state from circling bound pairs, as spinning here arises from thermal fluctuations (see also Supplementary Sec. 2). Notably, two scattering events occurred during the process (Fig. 1g), indicating thermal fluctuations enable transitions between circling and head-to-head states.

3 Attractive parallel scattering

Beyond head-on scattering, we extended our dimer model to parallel scattering of Janus colloids. Similarly, neighbor-induced concentration fields generate torque (Fig. 2a), with athermal dynamics categorized in Fig. 2b. Increasing the mobility contrast transforms repulsive scattering into parallel motion and then attractive scattering; further increases in μ_a/μ_p or d_c leads to circling bound states and ultimately static head-to-head state.

Thermal fluctuations render parallel motion a transient transition between repulsive and attractive scattering instead of a stable state, reducing the pink regime in the athermal state diagram (Fig. 2b) to a boundary. Fig. 2c and Supplementary Video S3 shows Brownian dynamics trajectories ($D/D_0 = 0.1$) for $d_c/r_p = 1.2$ and $\mu_a/\mu_p = 0.6$: parallel motion eventually terminates in attractive scattering, with shorter transient periods at higher μ_a/μ_p. Experimentally, standard Janus particles exhibit this parallel-to-attractive scattering transition (Fig. 2d; Supplementary Video S4). C_{o_1,o_2} shows uncorrelated orientations before encounter ($t = 1.7$ s); $C_{o_1,o_2} \approx 1$ during parallel motion, then gradually decreases to -1 — corresponding to antiparallel alignment during scattering (Fig. 2e).

Further increases mobility contrast to $\mu_a/\mu_p = 3$, parallel motion rapidly evolves into circling state, with particles rotating around a common center without contact (Fig. 2f; Supplementary Video S3). Experimentally, dewetted Janus particles exhibit this parallel-to-circling transition (Fig. 2g; Supplementary Video S4). Corresponding C_{o_1,o_2} values (Fig. 2h) remain near 1 during parallel motion, except during position swapping (visible in Fig. 2g), and converge to -1 after $t = 3.1$ s — consistent with circling, as further confirmed by positive angular velocity ω (Fig. 2h).

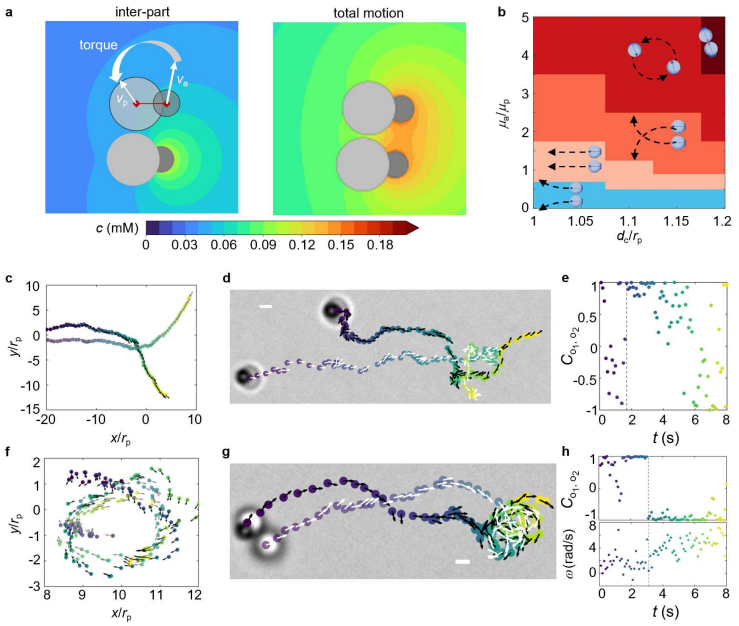


Fig. 2 Attractive parallel scattering. a Interaction between side-by-side moving Janus particles. The left schematic illustrates dimer–dimer interactions between two Janus particles with surface mobilities $\mu_a > \mu_p > 0$. **b** μ_a/μ_p vs. d_c/r_p state diagram from athermal simulations, showing repulsive scattering (blue), parallel motion (pink), attractive scattering (coral), circling bound state (red) and head-to-head static state (dark red). **c-e** Transition from parallel motion to attractive scattering. Simulation trajectories for particles with $d_c/r_p = 1.2$ and $\mu_a/\mu_p = 0.6$ (**c**); experimental trajectories for standard Janus particles (**d**) and the corresponding orientation correlation C_{o_1,o_2} (**e**). The dashed line marks particle encounter. **f-h** Transition from parallel motion to circling bound state. Simulation trajectories for particles with $d_c/r_p = 1.2$, $\mu_a/\mu_p = 3$ (**f**); experimental trajectories for dewetted Janus colloids (**g**) and the corresponding C_{o_1,o_2} and angular velocity ω (**h**). Dashed lines indicate the onset of circling motion. For all trajectories, arrows denote particle orientation. Scale bar: 1 μm.

4 Three particles swarming

In light of the recapturing behavior between Janus particles, we used the dewetted hematite/TPM system to construct long-term inter-particle motion, which should shed new light on constructing swarms from repulsive active particles. Fig. 3a and Supplementary Video 5 compare a free Janus particle with three "dancing" particles in situ: Particles 1 (blue) and 2 (orange) danced throughout the observation period, while Particle 3 (green) was slung away, swam independently for 12 s, then recaptured.

Orientation (C_o) and velocity direction (C_v) autocorrelation functions of dancing particles decayed faster than those of the free particle (Fig. 3b), demonstrating inter-particle interaction effects. The $\theta_{v,o}$ probability distribution in Fig. 3c was broader for dancing particles than for the free particle, which mostly self-propelled along its orientation. It also exhibited non-zero probability at $\pm 180°$, indicating velocity reversal arises from inter-particle interaction rather than thermal fluctuations.

Mean square displacement (MSD) of all particles (Fig. 3d) showed a slope of 2 ($\langle \Delta r^2 \rangle \sim v^2 \Delta t^2$), confirming their activities. Short-timescale individual velocities

decayed to long-timescale the cluster velocity, consistent with particles dancing around each other and moving slower than individually.

To understand this cluster dynamics, we simulated three Janus particles (P1, P2, P3) with the initial arrangement in Fig. 3e. No moving clusters formed when all three had identical surface properties. This is reasonable, as preferential directions are rare in near-symmetrical setups. Thus, P1 was fixed at $\{d_c/r_p, \mu_a/\mu_p\} = \{1.2, 1.2\}$, while P2 and P3 had $d_c/r_p = 1.2$ and varying μ_a/μ_p.

Athermal simulations (Fig. 3f, left to right: $\mu_a/\mu_p = 3, 4, 5$) showed distinct behaviors: $\mu_a/\mu_p = 3$ induced constant scattering with regular trajectories; $\mu_a/\mu_p = 4$ confined P2 and P3 within P1's trajectory; $\mu_a/\mu_p = 5$ formed a swarming cluster with periodic escape and recapture of P1.

Detailed analysis of $\mu_a/\mu_p = 5$ confirms that the simulation captures key experimental features. In Fig. 3g, gradual decay of C_o and C_v with long-timescale regular fluctuations indicates multi-periodic dynamics. The $\theta_{v,o}$ distribution shows small but non-zero probability at $\pm 180°$, consistent with experimental velocity reversal. The MSD in Fig. 3h qualitatively reproduces the experimental MSD (Fig. 3d), capturing the decay of short-timescale individual velocities to long-timescale cluster velocity—a key signature of coordinated particle motion.

Thermal effects were studied (Supplementary Sec. 3). Particle dynamics were dominated by μ_a/μ_p, while periodicity was suppressed by increasing thermal fluctuation. $\theta_{v,o}$ distributions for P2 (Fig. 3i) showed increasing $\pm 180°$ probability with μ_a/μ_p, regardless of fluctuation strength. It reconfirms velocity reversal originates from inter-particle interaction. Notably, thermal fluctuation extended P1's free-swimming time before recapture (Fig. 3j), qualitatively explaining enhanced recapture in experiments.

5 Velocity increment during scattering

Beyond the persistent directional motion of the three-particle cluster, the dramatic transient velocity enhancement observed in Supplementary Video S5 is intriguing. To characterize this dynamics, the transient velocities of dancing and free particles were plotted in Fig. 4a. The average transient velocities of dancing particles were $\bar{v}_1 = 7 \pm 5$ μm/s, $\bar{v}_2 = 6 \pm 3$ μm/s and $\bar{v}_3 = 6 \pm 3$ μm/s for particles 1, 2 and 3, respectively—close to that of the free particle ($\bar{v}_f = 5 \pm 2$ μm/s). The maximum transient velocity of particle 1 exceeded $4\bar{v}_1$. Further discussion of average velocity is provided in the Supplementary Sec. 4. Transient velocity enhancement arises from two configuration categories (Fig. 4b): the first, termed "slingshot-sideways", describes one particle accelerating as it passes the side of the other two; the second, "slingshot-in-between", involves one particle moving between the other two and being propelled away with high transient velocity.

The slingshot effect is rationalized by the model in Fig. 1a, with acceleration arising from close alignment of inter-particle (v_p and v_a) and self-propulsion velocities v via overlapping concentration fields. Simulations of three representative configurations (Fig. 4c, P1: {1.2, 1.2}; P2, P3: {1.2, 5}) confirm particle separation dominates velocity magnitude—closer spacing raises all particles' velocities due to a stronger concentration gradient. Swapping P1 and P2 positions changes all velocity, a direct

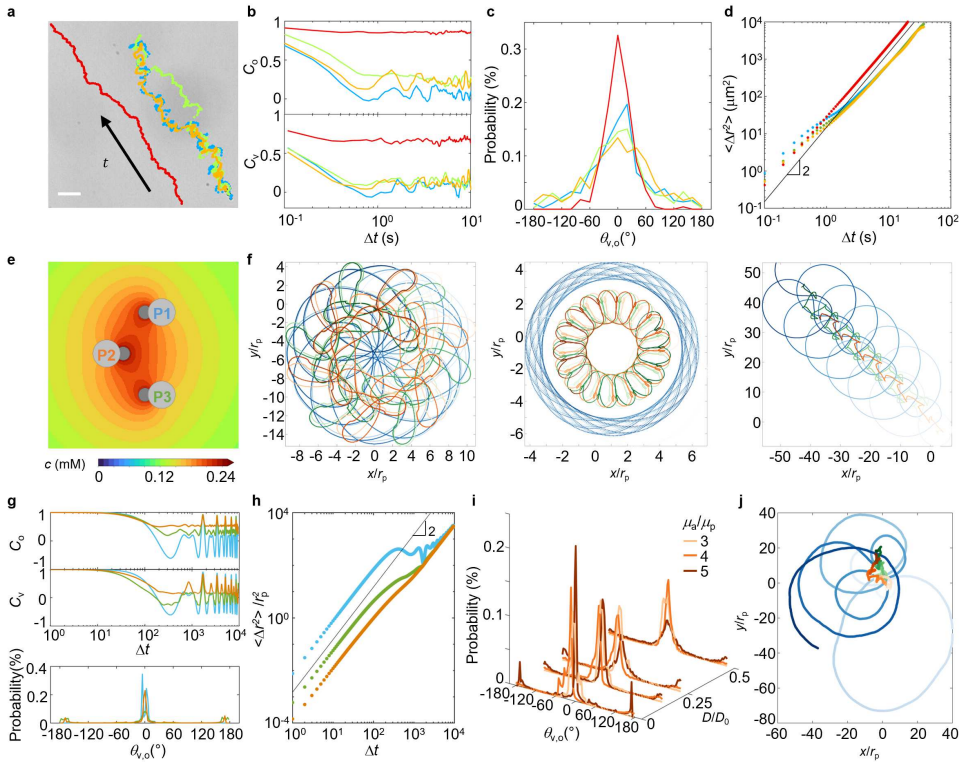


Fig. 3 Three colloids swarming. a - d, Experimental trajectories (**a**); autocorrelation functions of orientation C_{o} and velocity direction C_{v} (**b**); probability distribution of $\theta_{\mathrm{v,o}}$ (**c**); and mean square displacement (MSD) (**d**) of dancing particle 1 (blue), 2 (orange), 3 (green) and a free particle (red). **e**, Initial simulation configuration overlaid with the resulting concentration field. **f**, Athermal simulation trajectories for particle parameter sets (P1, P2, P3) = ({1.2, 1.2}, {1.2, 3},{1.2, 3}) (left), ({1.2, 1.2}, {1.2, 4},{1.2, 4}) (middle), ({1.2, 1.2}, {1.2, 5},{1.2, 5}) (right); time progresses as color transitions from transparent to opaque. **g - h**, Autocorrelation functions C_{o}, C_{v} and probability distribution of $\theta_{\mathrm{v,o}}$ (**g**); and MSD (**h**) of the swarming case ({1.2, 1.2}, {1.2, 5},{1.2, 5}). **i**, Probability distribution of $\theta_{\mathrm{v,o}}$ of particle 2 with varying $\mu_{\mathrm{a}}/\mu_{\mathrm{p}}$ and thermal fluctuation intensity D/D_0. **j**, Trajectories of dancing particles with parameters (P1, P2, P3) = ({1.2, 1.2}, {1.2, 5},{1.2, 5}) and thermal fluctuation intensity $D/D_0 = 0.05$.

manifestation of the non-reciprocal interactions. Though our 2D model neglects the fly off of the particle during slingshot-in-between events, it qualitatively captures the underlining physics.

The model in Fig. 1a further implies that transient acceleration can be induced by the passage of two particles. Therefore, we investigated the transient velocity during attractive scattering. The configuration of two scattering particles can be identified by their inter-particle distance d and the angles θ_1 and θ_2 between each particle's orientation and the center-to-center line (Fig. 4d); $\theta_{1,2} \in [-180, 180]$, with positive values for counter-clockwise. Simulation configurations can be defined analogously (Fig. 4e). Maximum velocity is expected when two anti-aligned particles have adjacent active faces, yielding the highest concentration gradient (Fig. 4f).

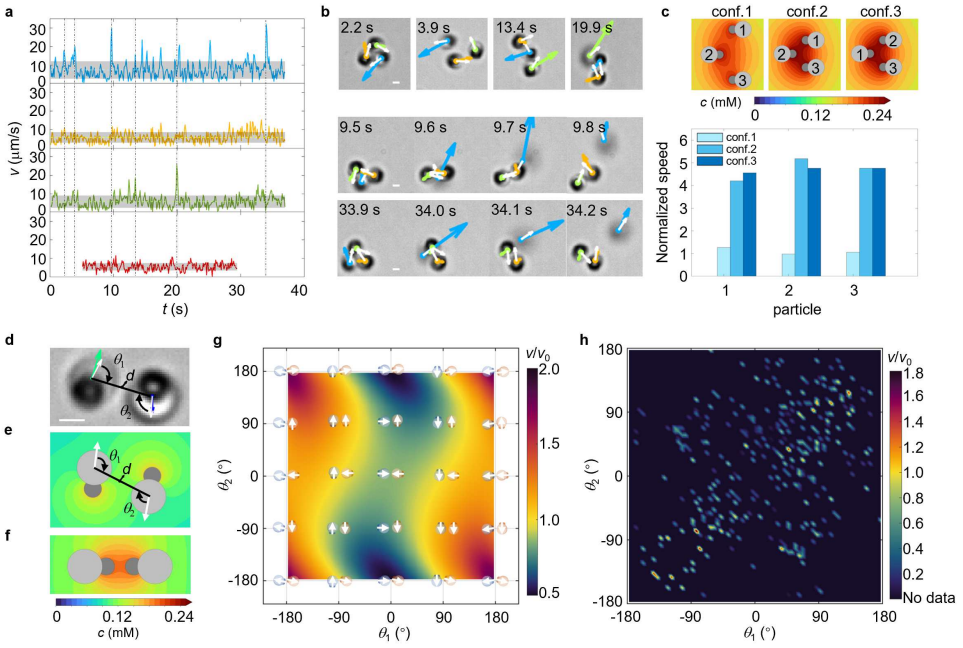


Fig. 4 Concentration slingshot effect. a, Transient speed of dancing particles and a free lancing particle. Vertical dashed lines denote times in **b**. Colored dashed line denotes the average speed of the particle and shaded areas correspond to one standard deviation. **b**, Colloidal configuration of slingshot-sideways (first row) and slingshot-in-between (second and third rows), marked with orientation (white arrows) and velocity (colored arrows). Color codes as in Fig. 3a. **c**, Concentration field of 3 Janus particles in different configurations and the speed normalized by corresponding single particle speed. **d - e**, d and θ_1, θ_2 identify the configuration during pairwise scattering in experiments (**d**) and simulation (**e**). **f - g**, With $d = 4r_\mathrm{p}$, the configuration that generates highest concentration gradient (**f**) and the normalized speed v/v_0 of two $\{d_\mathrm{c},\ \mu_\mathrm{a}/\mu_\mathrm{p}\} = \{1.2,\ 1\}$ particles vs. θ_1, θ_2 (**g**). Schematics of configurations were overlaid on the $\theta_1 \sim \theta_2$ plane. **h**, Experimental v/v_0 during scattering plotted against θ_1 and θ_2.

We simulated the speed of two particles with $\{1.2,\ 1\}$ in varying configurations. For a fixed separation $d = 4r_\mathrm{p}$, particle speed v normalized by single-particle speed v_0 is plotted against θ_1 and θ_2 in Fig. 4g. The plot is centrosymmetric, with maximum velocity ($\approx 2v_0$) at the four corners—consistent with the concentration field in Fig. 4f. Notably, the minimum velocity does not occur at the head-to-head configuration $(\theta_1, \theta_2) = (0, 0)$, owing to residual separation between the passive faces of the Janus particles. Instead, when two particles move in alignment with one chasing the other, the trailing particle $(0, \pm 180)$ exhibits the lowest velocity ($< 0.5v_0$), while the leading particle $(\pm 180, 0)$ is accelerated. This result is consistent with our dimer model and aligns with previous analytical study [12]: inter-particle motion opposes self-propulsion for the trailing particle, whereas the two motions align for the leading particle.

Experimentally, we only considered particle pairs with $d < 4r_\mathrm{p}$. Compiling results from all scattering events, v/v_0 was plotted against θ_1 and θ_2 in Fig. 4h. For identical configurations $(\theta_1,\ \theta_2)$, the two particles exhibit different velocities. Therefore,

data points in the θ_1 *vs.* θ_2 plane are symmetric about the line $\theta_1 = \theta_2$, with different corresponding velocity values. Acceleration increases with both $|\theta_1|$ and $|\theta_2|$, and experimental results show general agreement with the simulated trend, despite experimental complexity.

6 Janus colloids in an external gradient field

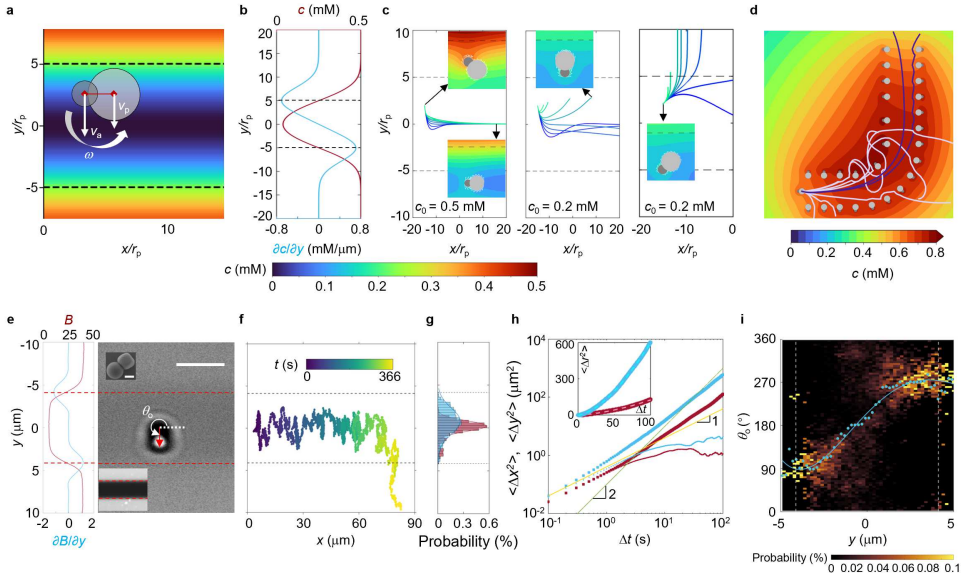


Fig. 5 Guiding motion with a boundary. a, Schematic of the dimer model in an external concentration field. **b**, The external concentration field with $c_0 = 0.5$ mM (red) and its gradient (blue) in the simulation. **c**, Athermal trajectories of Janus colloids with $d_c = 1.2$ and varying μ_a/μ_p in gradient fields of different c_0. From blue to cyan, $\mu_a/\mu_p = 0.5, 0.6, 0.7, 0.8, 0.9, 1.0, 1.5, 2.0$. All trajectories shares the same time span. The insets present the concentration field around the colloid with white arrows indicating the concentration gradient at the surface. Dashed lines in **a - c** denote the concentration boundaries. **d**, The athermal trajectories of a Janus colloids with $d_c = 1.1$ and $\mu_a/\mu_p = 0.5$, 0.6, 0.7, 0.81, 0.82, 1.0, 1.5, 2.0 (from top to bottom) in a colloidal highway formed by colloids of $d_c = 1.2$. **e**, Micrograph of a dumbbell particle moving in a structured light field with UV light of 0.66 mW/cm^2 that characterized by the brightness B (red) and its gradient $\partial B/\partial y$ (blue). The insets presents the SEM image of the particle (top, scale bar = 1 μm) and the structured light field (bottom). Scale bar = 5 μm. **f**, Trajectory of a dumbbell particle in structured light. **g**, Probability distribution function of y coordination of the paritcle in the dark strip with UV light of 0.66 mW/cm^2 (blue) and 1.09 mW/cm^2 (red). **h**, x (squares) and y (points) direction MSD of the dumbbell particle in light field with UV light of 0.66 mW/cm^2 (blue) and 1.09 mW/cm^2 (red). The inset presents the full MSD fitted to Eq. S2. **i**, The distribution of colloidal orientation θ_o in the light field. The mean value $\bar{\theta}_o$ were indicated by blue points and fitted to a 4th-order polynomials (blue line). Dashed lines in **e - g** and **i** denote the light boundaries.

The dimer model describes how Janus particles respond to external fields regardless of their origin. Here, we extend this framework beyond inter-particle interactions to study particle behavior in an external concentration gradient. Consider a Janus

particle in a low-concentration band $c_{\text{ext}}(y)$ that remains constant at c_0 for $|y| \geq y_0$ and decays non-linearly for $|y| < y_0$ over a characteristic length scale of δ, essentially forming a potential well in y direction (Fig. 5a and Methods). At low Reynold number, its gradient ∇c yields a force $\propto \mu \nabla c$ in the y direction. The resulting torque depends on both mobility contrast $\mu_{\text{a}}/\mu_{\text{p}}$ and the local concentration gradients at the active and passive surfaces, which are determined by c_0 and the decay profile within $|y| < y_0$.

When c_{ext} overwhelms the self-generated concentration field c_{self}, the particle swims along the band center ($y = 0$) and orients along the x axis. We tested this prediction using athermal simulations of Janus particles with activity $\alpha = 0.5\alpha_0$, $d_{\text{c}}/r_{\text{p}} = 1.2$ and varying $\mu_{\text{a}}/\mu_{\text{p}}$ in the band with $c_0 = 0.5$ mM, $y_0 = 5$ μm and $\delta = 4$ μm (Fig. 5a-b). As expected, all particles were forced to move along $y = 0$ regardless of mobility contrast (Fig. 5c, left panel).

Reducing c_{ext}, or equivalently increasing α, creates a competition between external and self-generated fields. When these fields balance at the particle surface, net velocity in the y-direction vanishes. At $c_0 = 0.2$ mM, particles with $\mu_{\text{a}}/\mu_{\text{p}} = 0.5, 0.6$ remained at $y = 0$, whereas those with $\mu_{\text{a}}/\mu_{\text{p}} = 0.7, 0.8$ escaped through the lower boundary (Fig. 5, middle panel). For $\mu_{\text{a}}/\mu_{\text{p}} > 0.9$, particles reoriented perpendicular to the upper boundary ($y/r_{\text{p}} = 5$) and stopped when self-propulsion balanced the external drift. This balance point shifted away from the boundary as $\mu_{\text{a}}/\mu_{\text{p}}$ increased, since higher μ_{a} requires lower ∇c_{ext} to maintain $v_{\text{a}} = \mu_{\text{a}} \nabla c_{\text{ext}}$. Simulations further reveal that trajectories are geometrically invariant when the ratio c_0/α is held constant, differing only in their temporal evolution, as confirmed by the scaling analysis of the governing equations (see Supplementary Sec. 5).

Initial orientation further modulates this behavior (Fig. 5c, right panel, and Supplementary Sec. 5.3). Under $c_0 = 0.2$ mM, particles initially pointing toward the upper boundary typically escaped, except at $\mu_{\text{a}}/\mu_{\text{p}} = 0.5$, the particle moved along the center; at $\mu_{\text{a}}/\mu_{\text{p}} = 2.0$, it stopped at the upper boundary.

Such concentration boundary can also be realized by two rows of active Janus particles. A "colloidal highway" formed by two rows of active particles with $d_{\text{c}}/r_{\text{p}} = 1.2$ can selectively filter passing particles. Fig. 5d presents trajectories for particles with $d_{\text{c}}/r_{\text{p}} = 1.1$ and varying mobility contrast, where only $\mu_{\text{a}}/\mu_{\text{p}} = 0.81$ and 0.82 successfully transited.

We experimentally realized this low-concentration band using a light pattern generated by a digital micromirror device (DMD, Fig. 5e, Methods and Supplementary Sec. 6). UV illumination decomposes H_2O_2 with rate $\propto$ light intensity I [38], producing ionic concentrations $c_{\text{H}^+} = c_{\text{OH}^-} \propto I \propto B$, where B is the image brightness (plotted in Fig. 5e together with its gradient in y). Dumbbell-shaped Janus particles with $\{1.46, 1.49\}$ (Supplementary Sec. 1) provided strong field response, while their large hematite exposure ensured sensitivity to weak intensities near the dark-band boundary. A representative trajectory under 0.66 mW/cm^2 UV showed a long-time boundary-following (356 s) before eventual escape (Fig. 5f).

Varying illumination intensity modulates confinement strength. At 0.66 mW/cm^2, the position distribution centered at -0.8 μm with broad variance, whereas 1.09 mW/cm^2 yields a narrower distribution centered at -0.2 μm (Fig. 5g). This shift

toward the center at higher intensity confirms that stronger external fields trap particles deeper in the potential well, while weaker fields permit balance positions nearer boundaries. The narrow distribution of y in the 1.09 mW/cm^2 pattern also confirmed the stronger confinement in this case.

MSD analysis validates this picture (Fig. 5h). The short-time MSD in both x and y direction exhibited a slope close to 1. At longer timescales, however, $\langle \Delta x^2 \rangle$ approached a slop of 2, confirming the particle mobility along the band, whereas $\langle \Delta y^2 \rangle$ plateaus, indicating confinement. Notably, The lower $\langle \Delta y^2 \rangle$ at 1.09 mW/cm^2 reflects stronger confinement, consistent with Fig. 5g.

The full MSD $\langle \Delta r^2 \rangle$ shown in the inset follows the Supplementary Eq. S2. Particle speed decreases from 0.51 μm/s (0.66 mW/cm^2) to 0.13 μm/s (1.09 mW/cm^2). This is coincide with the results shown in Fig. 5g, that particles at 1.09 mW/cm^2 reside in dimmer regions (band center) than those near boundaries at 0.66 mW/cm^2.

Fig. 5i presents particle orientation θ_o statistics across the dark band, revealing that particles align perpendicular to the boundary when approaching them. Considering the experimental mobility contrast $\mu_a/\mu_p = 1.49$, this result coincide with the simulation results.

7 Conclusions

We provide a general dimer model for tailoring motions of active Janus colloids. A Janus colloid responds to the total gradient field via a torque controlled by mobility contrast μ_a/μ_p and active–passive separation d_c. Our description focuses on phoretic inter-particle interactions (Fig. 1-2), yet can be readily extended to osmotic flows, as both rely on the overall concentration field [39]. While demonstrated here for chemical concentration gradients, this framework generalizes to any scalar field—whether thermophoretic steering toward heated particles [40], electrically aligned co-moving Pt/Au doublets [13], concentration-controlled light communication between bacteria and cargo [6], or rectified motion in optical landscapes [41]—providing a unified perspective on how broken symmetry translates directional motion.

The non-reciprocal nature of interactions emerges naturally from the dimer model, enabling applications to active–passive mixtures [42–45], symbiotic systems [46], and predator–prey dynamics [47]. Our study (Fig. 3-4) may also extend the torque-induced aggregation beyond induced-charge electrophoresis [48], and rationalize the velocity enhancement observed between synthetic nanomotors [18].

We further provide a proof-of-concept simulation showing that external fields can guide Janus colloids, and experimentally realize such control using light-induced concentration gradients (Fig. 5). In general, any gradient field that elicits different responses between the active and passive parts of a Janus particle generates the torque-driven mechanism identified here and can thus regulate particle behavior. This aligns with prior studies using chemically patterned substrates [49, 50], light-induced electric field [23], and physical wall that suppress ion diffusion [46]. The dimer model thus offers a unified framework for rational design of interactions and field-guided colloidal robotics.

8 Methods

8.1 Experimental methods

8.1.1 Preparation of Janus colloids

In our experiments, we studied the dynamics of hematite/TPM Janus particles with varying morphologies. Hematite particles were prepared using the sol-gel method [51]. 100 ml of 2 M $FeCl_3.6H_2O$ (p.a., Sigma-Aldrich) and 10 ml of DI water was mixed with 90 ml of 6 M NaOH (puriss, Sigma-Aldrich). The resulting gel was aged at 100 °C for 8 days. Longer aging time resulted in larger size of the particles. The particles were washed repeatedly with DI water and re-suspended to obtain 0.0125 g/ml aqueous suspension.

To encapsulate hematite partially with TPM, we followed a modified protocol [52]. Briefly, 1 ml of TPM (≥98% Sigma-Aldrich) was hydrolyzed in 10 ml DI water. 1 ml of the resulting hydrolyzed TPM was added to 13.0 ml DI water containing 0.1 ml hematite-suspension and 3.4 μL of ammonia solution (25% wt., Sigma-Aldrich). The mixture was left undisturbed for 30 min to allow the heterogeneous nucleation of TPM oil droplet on hematite particles. Morphology alteration can be achieved by the dewetting of TPM droplet before polymerization. To trigger dewetting, 150 μL 5% PF108 (Sigma-Aldrich) and 50 μL 37% HCl (Sigma-Aldrich) was added to the mixture and left for 2 min. Longer dewetting time resulted in the dumbbell shape. 10 mg 1-hydroxycyclohexyl phenyl ketone (HCPK) was added into the suspension before the polymerization under UV light at room temperature for 20 min. The products were washed in ethanol for 3 times then in DI water for 10 times.

The morphology of the resulting particles were characterized using a scanning electron microscope (ZEISS Sigma 360). The SEM images of the resulting standard hematite/TPM and dewetted particles were shown in the insets of Fig. 1d. The SEM image of the dumbbell particle was shown in the inset of Fig. 5e. The ζ potential of the active and passive component of the Janus colloids were characterized using Brookhaven Instruments NanoBrook 90Plus PALS. Details of the characterization can be found in Supplementary Sec. 1. The resulting d_c/r_p and μ_a/μ_p were summarized in Supplementary Table S1.

8.1.2 Microscopy observations

The Janus particles were suspended in an aqueous solution of 1% H_2O_2 and deposited on the glass substrate of a sample cell. A digital micromirror device (DMD, DLP6500, Texas Instruments) was coupled with the inverted microscope (Mingmei MF53) through the fluorescence light path using a tube lense. The DMD-modulated UV ($\lambda \approx 385$ nm) light beam is focused on the sample plane by a 60 × oil objective (Olympus, NA = 1.4). Particle dynamics were observed under a whit light bright-field using the same objective and imaged using a camera (Ximea MQ042MG-CM) with 10 Hz. Details of the optical setup are reported in Supplementary Sec. 6.

In particle interaction experiments (Fig. 1-3), a plain UV light field was used; while structured light was applied for boundary guided motion (Fig. 5) as described in Supplementary Sec. 6. We removed the emission filter in the filter cube, so that the UV

light reflected by the glass substrate of the sample cell can be imaged together with the transmitting white light when the focal plane was adjusted to the glass substrate. This enables the reposition of Janus colloids within the dark band. "Darkness" corresponds to transmitting white light but no UV illumination.

Particle location (center of the Janus particle) and orientation (pointing from hematite to TPM) were tracked using a MATLAB algorithm [53, 54]. The angle between orientation and velocity $\theta_{\mathrm{v,o}}$ can be determined, see Supplementary Fig. S2. For the cases when particle was shot off the substrate and out of focus, we determined the location of the particle by its projection and $\theta_{\mathrm{v,o}}$ was taken as zero.

8.2 Simulation methods

8.2.1 Calculation of concentration field

The concentration field around a Janus particle follows the Laplace's equation $\nabla^2 c = 0$ with a boundary condition $-D\mathbf{n}\cdot\nabla c = \alpha$, where α is the surface activity. We construct a complex potential of a Janus particle $F(z) = -\frac{M}{2\pi}\ln(z - z_{\mathrm{a}}) + \frac{De^{i\theta}}{z-z_{\mathrm{p}}} - F_\infty$ by assembling a point source of strength M (first term) at the active center z_{a} and a dipole of moment $De^{i\theta}$ close to the passive center z_{p}, where $z = x + iy$ is the coordinates of a location in the complex plane. The real ($c(z) = \mathrm{real}(F(z))$) and imaginary ($\psi(z) = \mathrm{imag}(F(z))$) part of $F(z)$, satisfies the Cauchy-Riemann condition: $\frac{\partial c}{\partial x} = \frac{\partial \psi}{\partial y}$, $\frac{\partial c}{\partial y} = -\frac{\partial \psi}{\partial x}$. Thus the stream function ψ automatically satisfies the Laplace's Equation $\nabla\psi = 0$. Therefore, the real part of $F(z)$ yields the concentration field with F_∞ enforcing $c \to 0$ at infinity. The stream function defines the boundary and center of Janus particle's passive part by adjusting D and z_{p} so that $|z - z_{\mathrm{p}}| = r_{\mathrm{p}}$.

To guide Janus particle motion, we employ a smoothed external field $c_{\mathrm{ext}}(y)$ forming a low-concentration band. We model this gradient field using the error function: $c_{\mathrm{ext}}(y) = \frac{c_0}{2}\left[\mathrm{erf}\left(\frac{y-y_0}{\delta}\right) - \mathrm{erf}\left(\frac{y+y_0}{\delta}\right)\right]$. Although demonstrated here for chemical concentration, this profile applies generally to thermal, optical, or electrical gradients.

The linearity of Laplace's equation allow as to evaluate the overall concentration field of multiple Janus particles by superposition of the complex potential of each particle j, i.e., $F_{\mathrm{tot}}(z) = \sum_j F_j(z) + c_{\mathrm{ext}}(z)$, so that $c = \mathrm{real}(F_{\mathrm{tot}}(z))$. Thus, $\frac{\partial c}{\partial x} = \mathrm{real}(\frac{\partial F}{\partial z})$ and $\frac{\partial c}{\partial y} = -\mathrm{imag}(\frac{\partial F}{\partial z})$, providing a simple way to evaluate the concentration gradient at the surface of Janus particles.

8.2.2 Brownian dynamics simulation

For each particle j, the governing equations of motion can be written as $\mathrm{d}\mathbf{r}_j/\mathrm{d}t = \mathbf{v}_j + \xi_j^{\mathrm{t}}(t)$, and $\mathrm{d}\mathbf{u}_j/\mathrm{d}t = \boldsymbol{\omega}_j \times \mathbf{u}_j + \xi_j^{\mathrm{r}}(t)$, $\mathbf{u}_j$ is the orientation of the particle. The translational and angular velocity of a Janus particle are given by $\mathbf{v} = -\frac{1}{S}\oint \mu(\mathbf{r}_{\mathrm{s}})(\mathbf{I} - \mathbf{nn})\cdot\nabla c(\mathbf{r}_{\mathrm{s}})ds$ and $\boldsymbol{\omega} = -\frac{1}{A}\oint \mathbf{r}\times\mu(\mathbf{r}_{\mathrm{s}})(\mathbf{I} - \mathbf{nn})\cdot\nabla c(\mathbf{r}_{\mathrm{s}})ds$, where S here is the total exposed perimeter of the particle, A is the two-dimensional rotational resistance coefficient of a disk [55]. $\xi_j^{\mathrm{t}}(t)$ and ξ_j^{r} are Gaussian noise with intensity of $2D^{\mathrm{t}}$ and $2D^{\mathrm{r}}$, which are scaled by the free translational $D_0 = \alpha_0\mu_0/24\pi$ and rotational $D_0^{\mathrm{r}} = \frac{3}{4r_{\mathrm{p}}^2}D_0$ diffusion coefficient, respectively, where α_0 and μ_0 are the surface activity and mobility of the active part [56].

Supplementary information. Supplementary videos and materials are provided in the Supplementary information.

Acknowledgements. This work was supported by the National Natural Science Foundation of China (12464027, 12304258), Guangxi Natural Science Foundation (2024GXNSFAA010215), the Wenner-Gren Foundation (UPD2023-0065), the Fundamental Research Funds for the Central Universities (PHD2023-012) and Youth Scientific Research and Innovation Team of Guangxi Science and Technology Normal University (GXKS2024QNTD07).

Declarations

9 Competing interests

The authors declare no competing interests.

10 Data availability

The data supporting the results in this study are available within the paper and its Supplementary Information. Source data are provided with this paper.

11 Author contributions

X.Z and L.L. conceived and supervised the project. X.Z. designed, conducted the microscopic experiments and led the data analysis. L.L. performed simulations and assisted with data analysis. W.L., S.W. and S.G. contributed to characterizations of Janus colloids and data analysis. F.Y. assisted with constructing the light control system. X.Z. wrote the paper with input from all authors.

12 Funding

Not applicable

13 Ethics approval and consent to participate

Not applicable

14 Consent for publication

Not applicable

15 Materials availability

Not applicable

16 Code availability

Not applicable

References

[1] Li, J., Ávila, B.E.F.D., Gao, W., Zhang, L., Wang, J.: Micro/nanorobots for Biomedicine: Delivery, surgery, sensing, and detoxification. Science Robotics **2**(4), 1–9 (2017) https://doi.org/10.1126/scirobotics.aam6431

[2] Lin, J., Guan, Q., Feng, J., Chen, S., Xu, L., Guan, J., Sánchez, S.: Interactions Between Active Matters and Endogenous Fields. Advanced Materials **03091**, 1–32 (2025) https://doi.org/10.1002/adma.202503091

[3] Urso, M., Ussia, M., Pumera, M.: Smart micro- and nanorobots for water purification. Nature Reviews Bioengineering **1**(4), 236–251 (2023) https://doi.org/10.1038/s44222-023-00025-9

[4] Chen, S., Fan, D.E., Fischer, P., Ghosh, A., Göpfrich, K., Golestanian, R., Hess, H., Ma, X., Nelson, B.J., Patiño Padial, T., Tang, J., Villa, K., Wang, W., Zhang, L., Sen, A., Sánchez, S.: A roadmap for next-generation nanomotors. Nature Nanotechnology **63**(January) (2025) https://doi.org/10.1038/s41565-025-01962-9

[5] Bishop, K.J.M., Biswal, S.L., Bharti, B.: Active Colloids as Models, Materials, and Machines. Annual Review of Chemical and Biomolecular Engineering **14**(1), 1–30 (2023) https://doi.org/10.1146/annurev-chembioeng-101121-084939

[6] Zheng, X., Zheng, Y., Heidari, A., Wegner, S.V.: Autonomous Cargo Transport with Biohybrid Microswimmers Enabled by Light-Mediated Bacteria-Cargo Communication. Advanced Materials, 1–12 (2026) https://doi.org/10.1002/adma.72950

[7] Sharifi-Mood, N., Mozaffari, A., Córdova-Figueroa, U.M.: Pair interaction of catalytically active colloids: from assembly to escape. Journal of Fluid Mechanics **798**, 910–954 (2016) https://doi.org/10.1017/jfm.2016.317 arXiv:1510.03000

[8] Reigh, S.Y., Chuphal, P., Thakur, S., Kapral, R.: Diffusiophoretically induced interactions between chemically active and inert particles. Soft Matter **14**(29), 6043–6057 (2018) https://doi.org/10.1039/c8sm01102h arXiv:1806.08643

[9] Nasouri, B., Golestanian, R., Exact Phoretic Interaction of Two Chemically Active Particles. Physical Review Letters **124**(16), 168003 (2020) https://doi.org/10.1103/PhysRevLett.124.168003

[10] Nasouri, B., Golestanian, R.: Exact axisymmetric interaction of phoretically active Janus particles. Journal of Fluid Mechanics **905**, 13 (2020) https://doi.org/10.1017/jfm.2020.753 arXiv:2005.09429

[11] Saha, S., Ramaswamy, S., Golestanian, R.: Pairing, waltzing and scattering of chemotactic active colloids. New Journal of Physics **21**(6), 063006 (2019) https://doi.org/10.1088/1367-2630/ab20fd

[12] Rojas-Pérez, F., Delmotte, B., Michelin, S.: Hydrochemical interactions of phoretic particles: A regularized multipole framework. Journal of Fluid Mechanics **919**, 1–31 (2021) https://doi.org/10.1017/jfm.2021.387 arXiv:2104.12396

[13] Wang, W., Duan, W., Sen, A., Mallouk, T.E.: Catalytically powered dynamic assembly of rod-shaped nanomotors and passive tracer particles. Proceedings of the National Academy of Sciences of the United States of America **110**(44), 17744–17749 (2013) https://doi.org/10.1073/pnas.1311543110

[14] Sharan, P., Daddi-Moussa-Ider, A., Agudo-Canalejo, J., Golestanian, R., Simmchen, J.: Pair Interaction between Two Catalytically Active Colloids. Small **19**(36), 0–13 (2023) https://doi.org/10.1002/smll.202300817

[15] Katuri, J., Poehnl, R., Sokolov, A., Uspal, W., Snezhko, A.: Arrested-motility states in populations of shape-anisotropic active Janus particles. Science Advances **8**(26), 1–12 (2022) https://doi.org/10.1126/sciadv.abo3604

[16] Jiang, H.R., Yoshinaga, N., Sano, M.: Active motion of a Janus particle by self-thermophoresis in a defocused laser beam. Physical Review Letters **105**(26), 1–4 (2010) https://doi.org/10.1103/PhysRevLett.105.268302 arXiv:1010.0470

[17] Yu, N., Shah, Z.H., Basharat, M., Wang, S., Zhou, X., Lin, G., Edwards, S.A., Yang, M., Gao, Y.: Active self-assembly of colloidal machines with passive rotational parts via coordination of phoresis and osmosis. Soft Matter **19**(48), 9505–9510 (2023) https://doi.org/10.1039/D3SM01451G

[18] Chen, C., Chang, X., Teymourian, H., Ramírez-Herrera, D.E., Esteban-Fernández de Ávila, B., Lu, X., Li, J., He, S., Fang, C., Liang, Y., Mou, F., Guan, J., Wang, J.: Bioinspired Chemical Communication between Synthetic Nanomotors. Angewandte Chemie - International Edition **57**(1), 241–245 (2018) https://doi.org/10.1002/anie.201710376

[19] Xie, H., Sun, M., Fan, X., Lin, Z., Chen, W., Wang, L., Dong, L., He, Q.: Reconfigurable magnetic microrobot swarm: Multimode transformation, locomotion, and manipulation. Science Robotics **4**(28), 8006 (2019) https://doi.org/10.1126/scirobotics.aav8006

[20] Yang, L., Jiang, J., Gao, X., Wang, Q., Dou, Q., Zhang, L.: Autonomous environment-adaptive microrobot swarm navigation enabled by deep learning-based real-time distribution planning. Nature Machine Intelligence **4**(5), 480–493 (2022) https://doi.org/10.1038/s42256-022-00482-8

[21] Ghellab, S.E., Al-salihi, M., Zhou, X., Lei, L., Yan, D.: Remotely Programmable Multicolor-Emitting Microswimmer with Switchable Propulsion Modes. Advanced Functional Materials **35**(42), 1–11 (2025) https://doi.org/10.1002/adfm.202504218

[22] Liu, Y., Pak, O.S., Tsang, A.C.H.: Learning to Navigate in Chemical Fields Without A Map at Low Reynolds Numbers. Advanced Science **10092**, 1–10 (2025) https://doi.org/10.1002/advs.202510092

[23] Chen, X., Chen, X., Elsayed, M., Edwards, H., Liu, J., Peng, Y., Zhang, H.P., Zhang, S., Wang, W., Wheeler, A.R.: Steering Micromotors via Reprogrammable Optoelectronic Paths. ACS Nano **17**(6), 5894–5904 (2023) https://doi.org/10.1021/acsnano.2c12811

[24] Arlt, J., Martinez, V.A., Dawson, A., Pilizota, T., Poon, W.C.K.: Painting with light-powered bacteria. Nature Communications **9**(1), 768 (2018) https://doi.org/10.1038/s41467-018-03161-8 arXiv:1710.08188

[25] Rey, M., Volpe, G., Volpe, G.: Light, matter, action: Shining light on active matter. ACS Photonics **10**(5), 1188–1201 (2023) https://doi.org/10.1021/acsphotonics.3c00140 https://doi.org/10.1021/acsphotonics.3c00140

[26] Che, S., Zhang, J., Mou, F., Guo, X., Kauffman, J.E., Sen, A., Guan, J.: Light-Programmable Assemblies of Isotropic Micromotors. Research **2022**, 1–12 (2022) https://doi.org/10.34133/2022/9816562

[27] Zehavi, M., Rachbuch, I., Park, S., Miloh, T., Velev, O.D., Yossifon, G.: Programmable Motion of Optically Gated Electrically Powered Engineered Microswimmer Robots. Small **21**(22), 1–10 (2025) https://doi.org/10.1002/smll.202501317

[28] Makey, G., Galioglu, S., Ghaffari, R., Engin, E.D., Yıldırım, G., Yavuz, Ö., Bektaş, O., Nizam, Ü.S., Akbulut, Ö., Şahin, Ö., Güngör, K., Dede, D., Demir, H.V., Ilday, F.Ö., Ilday, S.: Universality of dissipative self-assembly from quantum dots to human cells. Nature Physics **16**(7), 795–801 (2020) https://doi.org/10.1038/s41567-020-0879-8

[29] Heuthe, V.L., Iyer, P., Gompper, G., Bechinger, C.: Tunable colloidal swarmalators with hydrodynamic coupling. Nature Communications **16**(1) (2025) https://doi.org/10.1038/s41467-025-66830-5

[30] Anderson, J.: Colloid Transport By Interfacial Forces. Annual Review of Fluid Mechanics **21**(1), 61–99 (1989) https://doi.org/10.1146/annurev.fluid.21.1.61

[31] Zöttl, A., Stark, H.: Emergent behavior in active colloids (2016). https://doi.org/10.1088/0953-8984/28/25/253001 . https://iopscience.iop.org/article/10.1088/0953-8984/28/25/253001

[32] Moran, J.L., Posner, J.D.: Phoretic Self-Propulsion. Annual Review of Fluid Mechanics **49**(1), 511–540 (2017) https://doi.org/10.1146/annurev-fluid-122414-034456

[33] Howse, J.R., Jones, R.A.L.L., Ryan, A.J., Gough, T., Vafabakhsh, R., Golestanian, R.: Self-Motile Colloidal Particles: From Directed Propulsion to Random Walk. Physical Review Letters **99**(4), 8–11 (2007) https://doi.org/10.1103/PhysRevLett.99.048102

[34] Shah, Z.H., Wang, S., Xian, L., Zhou, X., Chen, Y., Lin, G., Gao, Y.: Highly efficient chemically-driven micromotors with controlled snowman-like morphology. Chemical Communications **56**(97), 15301–15304 (2020) https://doi.org/10.1039/d0cc06812h

[35] Kamp, M., Sacanna, S., Dullens, R.P.A.: Spearheading a new era in complex colloid synthesis with TPM and other silanes. Nature Reviews Chemistry **8**(6), 433–453 (2024) https://doi.org/10.1038/s41570-024-00603-4

[36] Palacci, J., Sacanna, S., Steinberg, A.P., Pine, D.J., Chaikin, P.M.: Living Crystals of Light-Activated Colloidal Surfers. Science **339**(6122), 936–940 (2013) https://doi.org/10.1126/science.1230020

[37] Zhou, X., Wang, S., Xian, L., Shah, Z.H., Li, Y., Lin, G., Gao, Y.: Ionic Effects in Ionic Diffusiophoresis in Chemically Driven Active Colloids. Physical Review Letters **127**(16), 168001 (2021) https://doi.org/10.1103/PhysRevLett.127.168001

[38] Savun-hekimoğlu, B.: Experimental and Theoretical Aspects of Azo Dye Degradation by UV/H2O2 Process: Review and experimental comparison of some kinetic rate expressions. International Journal of Environment and Geoinformatics **7**(3), 289–299 (2020) https://doi.org/10.30897/ijegeo.786158

[39] Wang, W.: Open Questions of Chemically Powered Nano- and Micromotors. Journal of the American Chemical Society **145**(50), 27185–27197 (2023) https://doi.org/10.1021/jacs.3c09223

[40] Rohde, L., Quinn, D., Paul, D., Cichos, F.: Regulated polarization of active particles in local osmotic flow fields. Communications Physics **8**(1), 213 (2025) https://doi.org/10.1038/s42005-025-02132-y

[41] Lozano, C., Hagen, B., Löwen, H., Bechinger, C.: Phototaxis of synthetic microswimmers in optical landscapes. Nature Communications **7**(1), 12828 (2016) https://doi.org/10.1038/ncomms12828

[42] Wang, Z., Wang, Z., Li, J., Cheung, S.T.H., Tian, C., Kim, S.H., Yi, G.R., Ducrot, E., Wang, Y.: Active Patchy Colloids with Shape-Tunable Dynamics. Journal of the American Chemical Society **141**(37), 14853–14863 (2019) https://doi.org/10.

1021/jacs.9b07785

[43] Wang, Z., Wang, Z., Li, J., Tian, C., Wang, Y.: Active colloidal molecules assembled via selective and directional bonds. Nature Communications **11**(1), 2670 (2020) https://doi.org/10.1038/s41467-020-16506-z

[44] Katuri, J., Uspal, W.E., Popescu, M.N., Sánchez, S.: Inferring non-equilibrium interactions from tracer response near confined active Janus particles. Science Advances **7**(18), 0719 (2021) https://doi.org/10.1126/sciadv.abd0719

[45] Zhang, J., Laskar, A., Song, J., Shklyaev, O.E., Mou, F., Guan, J., Balazs, A.C., Sen, A.: Light-Powered, Fuel-Free Oscillation, Migration, and Reversible Manipulation of Multiple Cargo Types by Micromotor Swarms. ACS Nano **17**(1), 251–262 (2023) https://doi.org/10.1021/acsnano.2c07266

[46] Wu, C., Dai, J., Li, X., Gao, L., Wang, J., Liu, J., Zheng, J., Zhan, X., Chen, J., Cheng, X., Yang, M., Tang, J.: Ion-exchange enabled synthetic swarm. Nature Nanotechnology **16**(3), 288–295 (2021) https://doi.org/10.1038/s41565-020-00825-9

[47] Mou, F., Li, X., Xie, Q., Zhang, J., Xiong, K., Xu, L., Guan, J.: Active Micromotor Systems Built from Passive Particles with Biomimetic Predator-Prey Interactions. ACS Nano **14**(1), 406–414 (2020) https://doi.org/10.1021/acsnano.9b05996

[48] Zhang, J., Alert, R., Yan, J., Wingreen, N.S., Granick, S.: Active phase separation by turning towards regions of higher density. Nature Physics **17**(8), 961–967 (2021) https://doi.org/10.1038/s41567-021-01238-8

[49] Uspal, W.E., Popescu, M.N., Dietrich, S., Tasinkevych, M.: Guiding Catalytically Active Particles with Chemically Patterned Surfaces. Physical Review Letters **117**(4), 1–5 (2016) https://doi.org/10.1103/PhysRevLett.117.048002 arXiv:1605.04246

[50] Huang, Y., Guo, J., Li, Y., Li, H., Fan, D.E.: 2D-Material-Integrated Micromachines: Competing Propulsion Strategy and Enhanced Bacterial Disinfection. Advanced Materials **2203082**, 1–10 (2022) https://doi.org/10.1002/adma.202203082

[51] Sugimoto, T., Sakata, K., Muramatsu, A.: Formation mechanism of monodisperse pseudocubic α-Fe2O3 particles from condensed ferric hydroxide gel. Journal of Colloid And Interface Science **159**(2), 372–382 (1993) https://doi.org/10.1006/jcis.1993.1336

[52] Youssef, M., Hueckel, T., Yi, G.-R., Sacanna, S.: Shape-shifting colloids via stimulated dewetting. Nature Communications **7**(1), 12216 (2016) https://doi.org/10.1038/ncomms12216

[53] Crocker, J.C., Grier, D.G.: Methods of Digital Video Microscopy for Colloidal Studies. Journal of Colloid and Interface Science **179**(1), 298–310 (1996) https://doi.org/10.1006/jcis.1996.0217

[54] Zhou, X.: Identifying the Orientation of Active Janus Colloids in Dilute Limit. 2023 2nd International Conference on Futuristic Technologies, INCOFT 2023, 1–5 (2023) https://doi.org/10.1109/INCOFT60753.2023.10425399

[55] Evans, E., Sackmann, E.: Translational and rotational drag coefficients for a disk moving in a liquid membrane associated with a rigid substrate. Journal of Fluid Mechanics **194**, 553–561 (1988) https://doi.org/10.1017/S0022112088003106

[56] Soto, R., Golestanian, R.: Self-assembly of catalytically active colloidal molecules: Tailoring activity through surface chemistry. Physical Review Letters **112**(6), 1–5 (2014) https://doi.org/10.1103/PhysRevLett.112.068301 arXiv:1306.6596

Supplementary Files

This is a list of supplementary files associated with this preprint. Click to download.

- VideoS5Threecolloidsswarming.avi
- VideoS2Headonscatteringfromexperiment.mp4
- NNSI.pdf
- VideoS3Parallelscatteringfromsimulation.mp4
- VideoS4Parallelscatteringfromexperiment.mp4
- VideoS1Headonscatteringfromsimulation.mp4
- VideoS6Bounaryguidedmotion1.avi